Scaling behavior of order parameters for the hybrid improper ferroelectric $(Ca, Sr)_3Ti_2O_7$

Jing Kong,[1] Alicia Manjón-Sanz,[2] Jue Liu,[2] Frederick Marlton,[3] Tsz Wing Lo,[1] Dangyuan Lei,[1] Mads Ry Vogel Jørgensen,[4,5] and Abhijit Pramanick[1,6,*]

[1]*Department of Materials Science and Engineering, City University of Hong Kong, Hong Kong, China*
[2]*Neutrons Scattering Division, Oak Ridge National Laboratory, Oak Ridge, Tennessee 37831, USA*
[3]*School of Mathematical and Physical Sciences, The University of Technology Sydney, Sydney NSW 2007, Australia*
[4]*Department of Chemistry and iNANO, Aarhus University, 8000 Aarhus C, Denmark*
[5]*MAX IV Laboratory, Lund University, SE-221 00 Lund, Sweden*
[6]*Center for Neutron Scattering, City University of Hong Kong, Hong Kong, China*

(Received 18 November 2022; revised 15 May 2023; accepted 24 May 2023; published 8 June 2023)

We show that in contrast to the conventional view of a mean-field Landau-type behavior, the oxygen octahedral tilt (R) and polarization (P) in the $A_3B_2O_7$ Ruddlesden-Popper hybrid improper ferroelectric $(Ca, Sr)_3Ti_2O_7$ exhibits the scaling behavior of a 2D Ising class near the para-to-ferroelectric transition temperature (T_c). We also show that P exhibits an additional transition from a 2D Ising to a 3D mean-field critical behavior at a temperature $T_d < T_c$, which is driven by enhanced interlayer dipolar correlations due to an increase in the ferroelectrically active B-site centered dipoles.

DOI: 10.1103/PhysRevB.107.224103

I. INTRODUCTION

In many ABO_3 ferroelectric materials, such as $BaTiO_3$, $PbTiO_3$, or $BiFeO_3$, the spontaneous polarization predominantly arises due to off-centering cation displacements [1] as a result of electronic phenomena such as Jahn-Teller distortions or lone-pair effects [2,3]. A complementary picture for polar displacements in perovskite crystals is that of lattice instabilities due to soft-phonon modes [1], which can ultimately be linked to such above electronic phenomena [2,3]. Nevertheless, such chemical bonding effects limit the scope for designing new ferroelectrics for applications, such as piezoelectric sensors, electrocaloric refrigeration, and nonvolatile memories [4,5]. In recent years, the discovery of hybrid improper ferroelectrics (HIF) has broadened the range of possible ferroelectrics, since they principally rely on nonelectronic geometric effects, such as tilting or rotation of the oxygen octahedra to induce cation displacements [6–8]. However, a lack of clear understanding of the phase-transition mechanisms in HIFs has constrained their rational design. The key to understanding the phase-transition mechanism in a material system is to characterize the temperature-dependent evolution of its order parameter(s) [1], which has not been examined comprehensively for HIFs. For example, it is debatable whether the transition to a polar phase is first- or second order in HIFs [7–10]. Additionally, it is not clear whether or not the evolution of polarization (P) can be always described by classical mean-field behavior for HIFs, which assumes the dominance of long-range interactions over short-range fluctuations [11,12]. Here, we examined these questions for the Ruddlesden-Popper (RP)-phase HIFs of $(Ca, Sr)_3Ti_2O_7$.

The potential for robust ferroelectric properties in RP oxides has generated great interest in these materials [6,13]. For example, theoretical calculations predicted a polarization $P \sim 20\,\mu C\,cm^{-2}$ for the RP $Ca_3Ti_2O_7$ [6], while experimental studies demonstrated switchable P of $\sim 0.6\,\mu C\,cm^{-2}$ [14] and $\sim 6\,\mu C\,cm^{-2}$ [15] for polycrystalline and single-crystalline $Ca_3Ti_2O_7$, respectively. The crystal structure of RP oxides $A_{n+1}B_nO_{3n+1}$ consists of blocks of n perovskite-like ABO_3 (or ABO_3) layers that are further separated by intervening AO (or A_2O) layers with the rocksalt structure in Fig. 1(a). As proposed by Benedek and Fennie [6], the high-temperature nonpolar $I4/mmm$ structure of RP oxides, such as $CaTi_3O_7$ and $Ca_2Mn_3O_7$, transforms to the ferroelectric $A2_1am$ structure via a simultaneous condensation of two octahedral distortions: (i) an in-phase rotation (θ_r) around the [001] axis or $a^0a^0c^+$ as per Glazer notation, and (ii) an out-of-phase tilt (θ_t) around the [110] axis or $a^-a^-c^0$. The primary order parameter (OP) for the paraelectric-to-ferroelectric phase transition is proposed to be the oxygen octahedral tilting/rotation distortions. In contrast, P constitutes the secondary OP, which means that the polar distortion is not the primary driver for the phase transition, but rather arises as a consequence of octahedral tilting/rotation. However, a fortuitous condensation of two lattice modes—octahedral tilting and rotation—at the ferroelectric transition temperature is not typical for Landau theory. Indeed, diffraction measurements have failed to show a direct transition from $I4/mmm$ to $A2_1am$ structure at the paraelectric-ferroelectric phase transition for many of the RP oxides [8–10,16–19]. Additionally, the temperature-dependent evolution of P is quite diverse in different RP phase ferroelectrics such as reported in Refs. [6,9,16,18], which raises the important question of whether a Landau-type model could be used to describe the behavior of all HIFs.

Here, we used high-resolution time-of-flight neutron-scattering experiments for a detailed structural characterization of the phase-transition parameters in $Ca_3Ti_2O_7$ and $Ca_{2.4}Sr_{0.6}Ti_2O_7$ RP oxides. We show that the evolution of

*apramani@cityu.edu.hk

 ©2023 American Physical Society

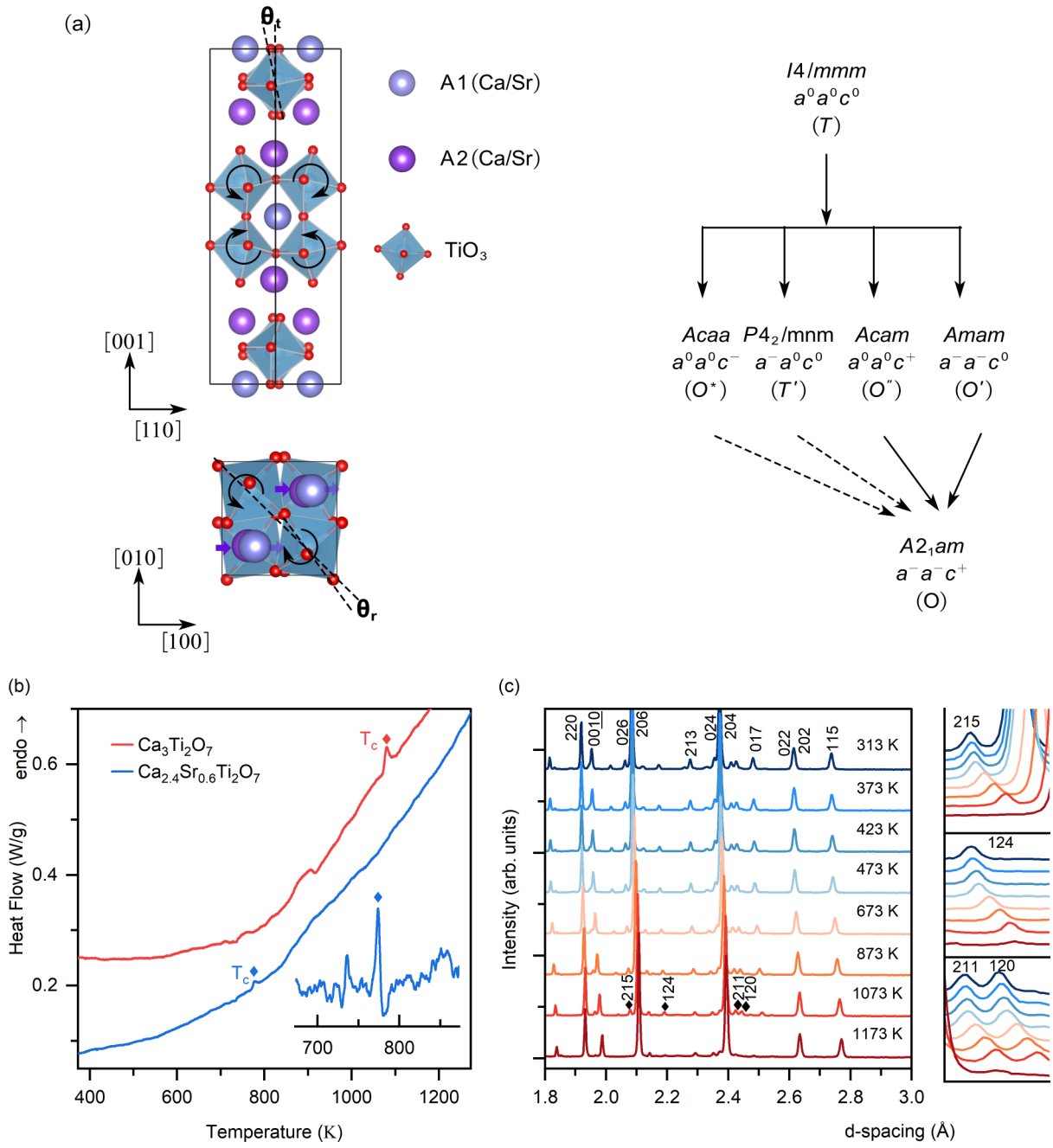

FIG. 1. (a) Crystal structure of $(Ca, Sr)_3Ti_2O_7$ with possible ferroelectric-paraelectric phase-transition pathways. Solid and dotted lines represent transitions with and without group-subgroup relations, respectively. (b) DSC curves of $Ca_3Ti_2O_7$ and $Ca_{2.4}Sr_{0.6}Ti_2O_7$ on heating. Both curves show small endothermic peaks, which mark the phase-transition temperatures, T_c. In addition, the slopes of the curves change above the temperature, T_d (see text for explanation). (c) Temperature-dependent neutron diffraction patterns of $Ca_3Ti_2O_7$. *hkl* reflections are indexed based on the $A2_1am$ structure. Diamonds indicate changes in *hkl* peak profiles.

neither R nor P follows mean-field Landau-type behavior, but rather exhibits the scaling behavior of a 2D Ising class near the para-to-ferroelectric transition temperature (T_c). More importantly, there is a second transition temperature, $T_d < T_c$, below which the temperature-dependent evolution of P transforms from that of a 2D Ising system to that of a 3D universality class. Such a change in the universality class arises due to the increased magnitude of the Ti-O polarization dipoles at lower temperatures, which increases the interlayer dipolar coupling. We propose that the transition in critical behavior below T_d may be a general feature for layered perovskite compounds with a ferroelectrically active B-site ion.

II. RESULTS AND DISCUSSION

Figure 1(a) illustrates the proposed mechanisms for paraelectric-to-ferroelectric transition in $(Ca, Sr)_3Ti_2O_7$. The high-temperature phase of $Ca_3Ti_2O_7$ has the $I4/mmm$ tetragonal (T) structure with no octahedral tilt or rotation. The different possible distortions of the T phase are the $Acaa$ (O^*),

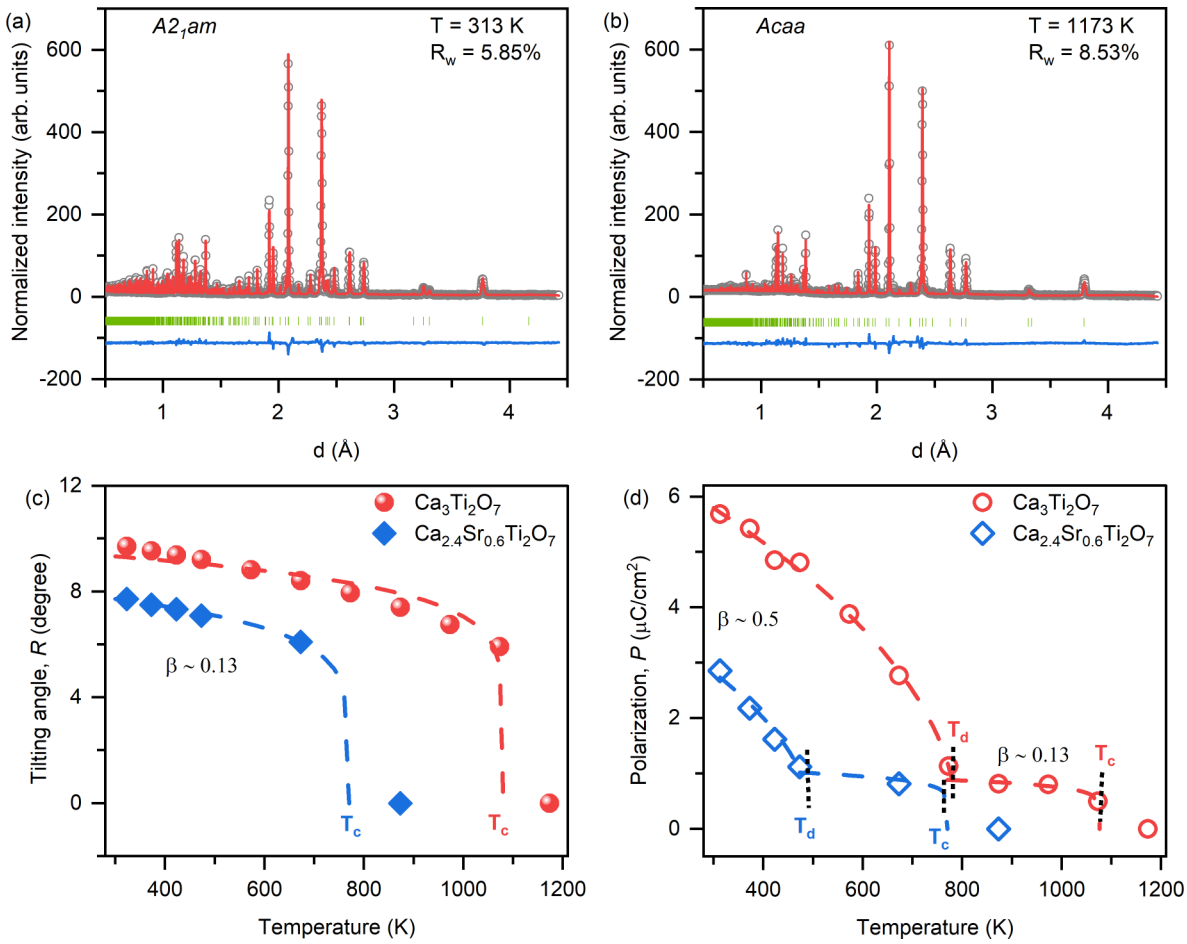

FIG. 2. (a), (b) Rietveld refinement fits of neutron diffraction patterns of $Ca_3Ti_2O_7$ measured at (a) 313 K and (b) 1173 K. Figures show the measured (black symbol), refined (red line), and difference (blue line) profiles, while Bragg peak positions are indicated by green tick marks. (c), (d) Temperature-dependent evolution of (c) primary OP, R, and (d) secondary OP, P. Both parameters are obtained from Rietveld refinement against Bragg diffraction data. Dotted lines show the fits using the equation $R \sim t^{\beta}$ or $P \sim t^{\beta}$, where $t = (T_c - T)$ and β is the critical exponent.

$P4_2/mnm$ (T'), $Acam$ (O''), and $Amam$ (O') space-group structures, or $a^0a^0c^-$, $a^-a^0c^0$, $a^0a^0c^+$, and $a^-a^-c^0$, respectively, in the Glazer notation [8,10,19,20]. As per some earlier studies, the paraelectric $I4/mmm$ structure transitions to the ferroelectric $A2_1am$ structure ($a^-a^-c^+$) through an intermediate paraelectric phase with $Acaa$ space-group structure ($a^0a^0c^-$) [10,16]. The transition between O and O^* phases is supposed to be first order due to a lack of group-subgroup relation; however, some x-ray and computational studies indicate that the structural transition in Sr-doped $Ca_3Ti_2O_7$ may be close to second order [10,16]. To verify this, we undertook differential scanning calorimetry (DSC) measurements for both $Ca_3Ti_2O_7$ and $Ca_{2.4}Sr_{0.6}Ti_2O_7$ upon heating [Fig. 1(b)]. For $Ca_3Ti_2O_7$, a clear endothermic peak is observed at $T_c \sim 1082$ K. For $Ca_{2.4}Sr_{0.6}Ti_2O_7$, while the original DSC curve does not show a distinct peak, the differential curve (shown in the inset) shows an anomaly at $T_c \sim 773$ K. These observations suggest that the ferro-to-paraelectric transition for both $Ca_3Ti_2O_7$ and $Ca_{2.4}Sr_{0.6}Ti_2O_7$ are first order, although the magnitude of the observed anomalies indicates that the transition is close to second order. The phase-transition temperatures, T_c, are also confirmed by Bragg diffraction measurements (see below). We additionally can note that the DSC curves show a change in their slopes at higher temperatures, which indicates structural relaxation. This is prominently observed for $Ca_3Ti_2O_7$, whereby the heat flow sharply increases above 800 K. For $Ca_{2.4}Sr_{0.6}Ti_2O_7$, the slope of the heat-flow curve changes more gradually beyond 500 K.

We examined the structural changes associated with the observed temperature-dependent anomalies in the DSC curve from analysis of neutron Bragg diffraction data, which were measured at the POWGEN instrument [21] (see Sec. S.1 in Supplemental Material (SM) [22] for details). Figure 1(c) shows that the temperature-dependent neutron-diffraction patterns of $Ca_3Ti_2O_7$ for $T \leqslant 1073$ K are similar, while a sharp decrease in the intensities of several reflections, such as *215, 124,* etc. can be observed at $T = 1173$ K indicating a phase transition. For $Ca_{2.4}Sr_{0.6}Ti_2O_7$, the diffraction patterns (Fig. S1 in SM) are similar for $T \leqslant 673$ K, while progressive changes in some of the peak intensities are observed at $T = 873$ K and $T = 1073$ K.

For structural characterization, we carried out Rietveld refinement against the measured Bragg diffraction data using the software GSAS-II [23]. The structural parameters, viz.,

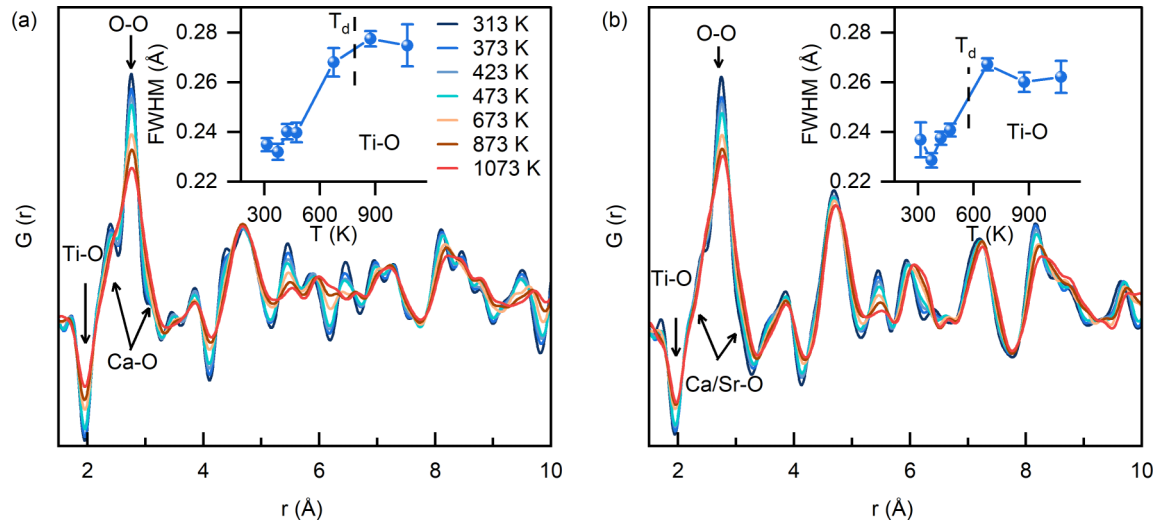

FIG. 3. Temperature-dependent evolution of $G(r)$ of (a) $Ca_3Ti_2O_7$, and (b) $Ca_{2.4}Sr_{0.6}Ti_2O_7$. Insets show the FWHM of the Ti-O peak as a function of temperature.

unit-cell parameters, atomic coordinates, and atomic displacement parameters, were refined to best fit the experimental diffraction patterns. The quality of the fits was assessed from the weighted residuals R_w [24]. Figures 2(a) and 2(b) show representative fits to the diffraction patterns of $Ca_3Ti_2O_7$ measured at 313 and 1173 K, respectively. The fits for all other temperatures and the detailed structural parameters are provided in the SM (Figs. S2 and S3) [22]. The diffraction peaks of $Ca_3Ti_2O_7$ for $T \leqslant 1073$ K can be reproduced well with a polar $A2_1am$ space-group structure. For the $T = 1173$ K pattern, Rietveld refinement using the different possible space groups]such as those indicated in Fig. 1(a)] showed that the best fit is obtained for the *Acaa* space group (Fig. 2(b) and Fig. S4 in SM [22]). Similarly, for $Ca_{2.4}Sr_{0.6}Ti_2O_7$, the measured diffraction patterns for $T \leqslant 673$ K are also reproduced well by the $A2_1am$ space group; see Fig. S5 in SM [21]. However, for $T = 873$ K, the best fit is obtained for the structure with the *Acaa* space group; see Fig. S6 in SM [22]. For the $T = 1073$ K pattern, the best fit is obtained with *I*4/*mmm* space group, while including the lowest number of variables; see Fig. S7 in SM [22]. These results confirm that for both $Ca_3Ti_2O_7$ and $Ca_{2.4}Sr_{0.6}Ti_2O_7$, the $A2_1am$-to-*I*4/*mmm* transition proceeds through an intermediate phase with the *Acaa* structure, which is equivalent to $a^-a^-c^+ \rightarrow a^0a^0c^- \rightarrow a^0a^0c^0$. In other words, the ferroelectric-paraelectric phase transition involves first a loss in octahedral tilting, followed by a loss in octahedral rotation. Therefore, we assert that octahedral tilting should be the primary order parameter, *R*. In addition, we observe nonlinear increases in atomic U_{iso} above T_c; see Fig. S8 in SM [22], which further supports the first-order nature of the ferroelectric-paraelectric phase transitions in $Ca_3Ti_2O_7$ and $Ca_{2.4}Sr_{0.6}Ti_2O_7$.

Figure 2(c) shows the temperature-dependent values of the octahedral tilt angle, which are obtained from Rietveld refinement, and constitute the primary OP, *R*. For both the compounds, *R* shows a continuous decrease with increasing temperatures up to T_c. Figure 2(d) shows the secondary OP, *P*, which was calculated from the refined structures against the Bragg diffraction data (for details, see Sec. S.4 in SM [22]). In contrast to *R*, *P* exhibits sharp changes at temperatures marked as T_d: $T_d \sim 800$ K for $Ca_3Ti_2O_7$ and $T_d \sim 500$ K for $Ca_{2.4}Sr_{0.6}Ti_2O_7$. Note that these temperatures roughly correspond to the points where we can observe increases in the slope of the heat-flow curves [Fig. 1(b)].

The peculiar nature of the different temperature-dependent behaviors of *R* and *P* can be explained based on their critical behavior. Ferroelectrics are known to exhibit certain types of critical behavior below T_c, which characterize different universality classes [25–29]. The universality class can be examined from the temperature dependence of OP, susceptibility, or correlation lengths [30,31]. Here, the experimentally determined OPs are fitted using the equation $R \sim t^\beta$ and $P \sim t^\beta$, where $t = (T_c - T)$ and β is the critical exponent. For both $Ca_3Ti_2O_7$ and $Ca_{2.4}Sr_{0.6}Ti_2O_7$, *R* could be fitted with the exponent $\beta \sim 0.13$ [Fig. 2(c)], which is close to the expected value of $\beta \sim 0.125$ for a two-dimensional Ising universality class. For context, $\beta \sim 0.5$ in the case of classical mean-field behavior for Landau theory of phase transition. This shows that the primary OP for the paraelectric-to-ferroelectric transition exhibits behavior that is unlike classical mean-field theory, but instead can be described by a 2D Ising universality class [30,31]. The 2D nature of the critical behavior for *R* is justified by the fact that the octahedral tilt orders couple more strongly within each perovskite ABO_3 layer, rather than across the intervening *A*O layers.

Notably, for $Ca_3Ti_2O_7$, the temperature dependence for *P* is not uniform below T_c. Near T_c, *P* can be fit using a critical exponent of $\beta \sim 0.13$ (similar to *R*), Fig. 2(d). However, *P* increases sharply below $T_d \sim 800$ K, at which point the best fit is obtained using $P \sim (T_d - T)^{0.5}$, which is expected for either mean-field behavior or 3D Ising model with correlated disorder [30,31]. For $Ca_{2.4}Sr_{0.6}Ti_2O_7$, a similar temperature-dependent behavior of *P* is observed, albeit with different transition temperatures T_c and T_d. The sharp change in *P* at T_d, which also correlates with an increase in heat flow, can be explained as a result of a transition from a 2D to a 3D universality class. Such a transition does not entail a crystallographic phase transition, but rather corresponds to

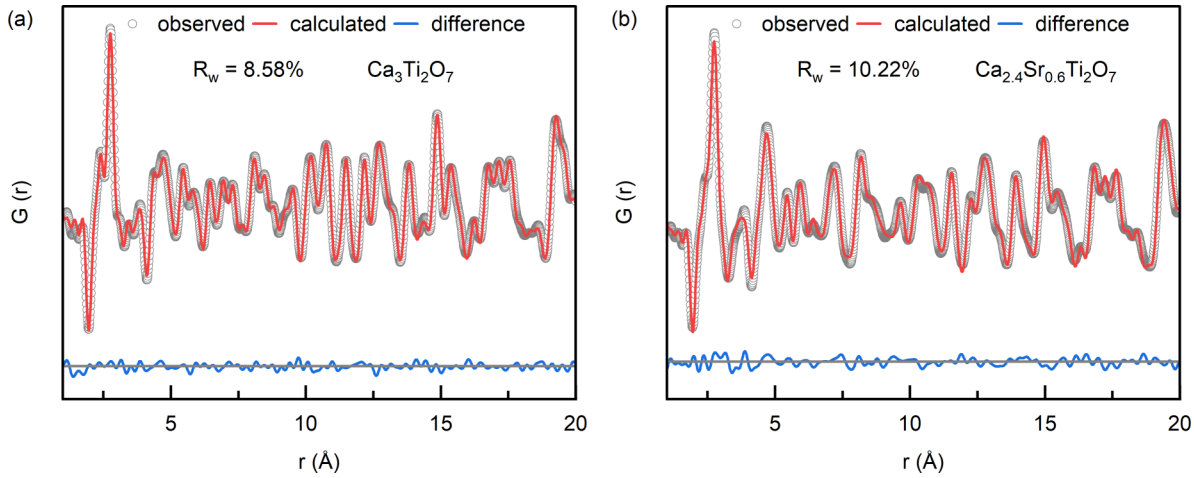

FIG. 4. (a), (b) Experimental and fitted $G(r)$ profiles of (a) $Ca_3Ti_2O_7$ and (b) $Ca_{2.4}Sr_{0.6}Ti_2O_7$ for interatomic distance $r \sim 20$ Å at 313 K.

how the electric dipoles couple in space, as further explained below.

In order to examine the structural origin of the temperature dependent behavior of P, we characterized the local dipole moments of Ca(Sr)-O and Ti-O. The local dipole moments were calculated from pair-distribution function (PDF) analyses of the neutron total scattering data [32] measured on NOMAD [33]. The temperature-dependent $G(r)$ for $Ca_3Ti_2O_7$ and $Ca_{2.4}Sr_{0.6}Ti_2O_7$ are shown in Figs. 3(a) and 3(b), respectively. For both compositions, we can note an increase in the peak widths with increase in temperature. For example, the insets in Figs. 3(a) and 3(b) show the full width at half maxima (FWHM) of the Ti-O peaks as a function of temperature. The FWHM increases with temperature indicating a steady increase in increasing disorder until T_d, beyond which the FWHM saturates. For quantitative analysis, the experimental $G(r)$ at different temperatures were fit using the software PDFGUI [34] (see details in Secs. S.3 and S.4 in SM [22]).

As shown in Figs. 4(a) and 4(b), the measured neutron PDF at 313 K for both $Ca_3Ti_2O_7$ and $Ca_{2.4}Sr_{0.6}Ti_2O_7$ in the range of $r < 20$ Å, can be fit using the $A2_1am$ structures. Furthermore, as shown in Figs. S11 and S12 [22], all the PDFs measured below T_c could be fit using the $A2_1am$ structure models. For $Ca_3Ti_2O_7$, reliable PDF data were not collected for temperatures above 1100 K. However, for $Ca_{2.4}Sr_{0.6}Ti_2O_7$, it is observed that the PDFs measured above $T_c \sim 773$ K are best fit with the nonpolar $Acaa$ structure (see Figs. S13 and S14 in SM [22]). This indicates that the temperature-dependent local structural evolution is similar to that observed for the average structure.

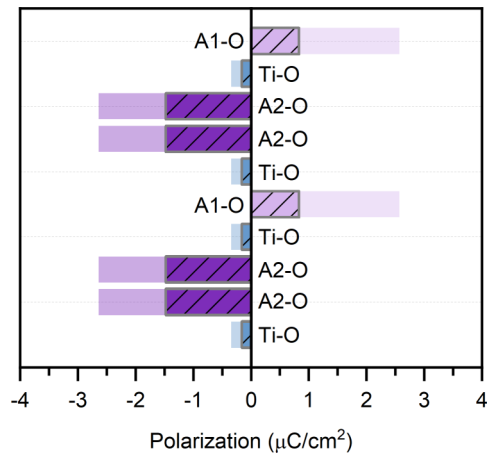

FIG. 5. Layer-by-layer contribution of polarization in $Ca_3Ti_2O_7$ and $Ca_{2.4}Sr_{0.6}Ti_2O_7$ at 313 K along the a axis, which was estimated from the local structure obtained from PDF analysis. Note that the light shade represents the dipole moments of $Ca_3Ti_2O_7$ and the dark shade with slashes represents the dipole moments of $Ca_{2.4}Sr_{0.6}Ti_2O_7$.

Based on the PDF refinement, we calculated the individual contributions of the Ca(Sr)-O and Ti-O dipoles to the net polarization. The temperature-dependent polarization is calculated from the refined atomic structural parameters. Since $(Ca, Sr)_3Ti_2O_7$ can be divided into the Ca/Sr1-O (or $A1$-O), Ti-O, and Ca/Sr2-O (or $A2$-O) electric dipole layers stacked along [001], the polarization for each layer is calculated separately, using the relation $P = \frac{ne}{V}\sum_i(\Delta r_i)$ where e is the elementary electronic charge, V is the volume of the unit cell, Δr is the displacement of the cation, Ca/Sr or Ti, from the center of its nearest-neighbor O atoms within each layer [35]. For Ca/Sr-O dipole layers, each Ca/Sr is coordinated to 4 O atoms as their nearest neighbors. For Ti-O dipole layers, each Ti is coordinated to 4 O atoms as their nearest neighbors. Therefore, $n = 4$ for the Ca/Sr-O dipoles and the Ti-O dipoles. Note that the dipoles in each layer along the b axis and c axis will cancel with each other, and therefore the net polarization is along the a axis. Figure 5 shows the layer-by-layer polarization for the average and local structures of both the compounds at 313 K. With respect to the reference of the figure, the $A2$-O and Ti-O layers contribute positively to the net P, while $A1$-O contributes negatively. The calculated total polarization of the local structure and average structures slightly differ, but show similar contributions from A-O and Ti-O dipoles (see Fig. S15 in SM [22]). Our calculated values for the total polarization are lower than those by Senn *et al.* [8]; however, the current values are consistent with the experimentally measured values of P by Oh *et al.* [15].

Figures 6(a) and 6(b) show the contributions to the total polarization from the A-O and Ti-O dipoles, as a function of temperature. The most notable features in Figs. 6(a) and

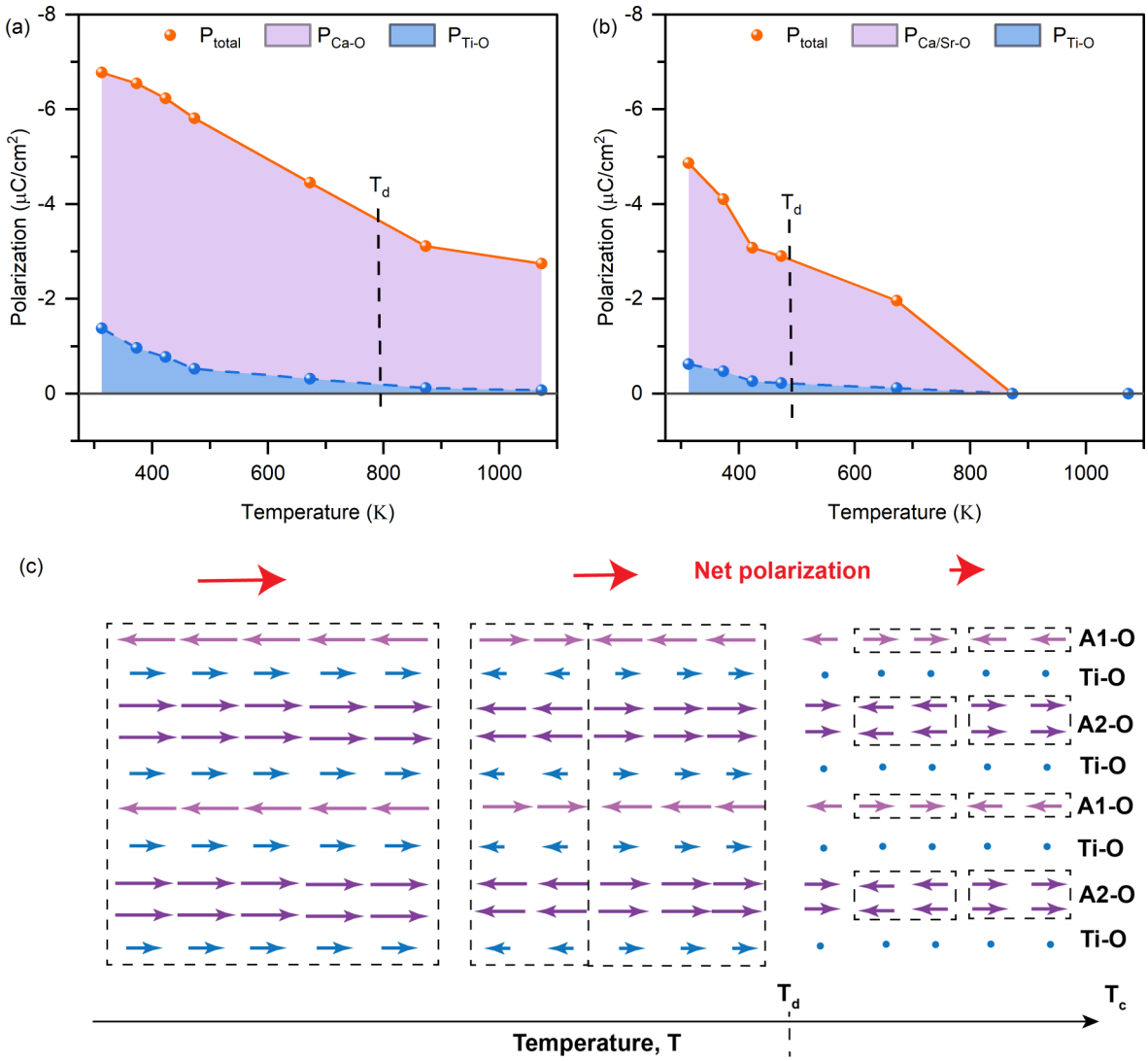

FIG. 6. Contributions to the total polarization from the local Ca/Sr-O and Ti-O dipoles, calculated from analysis of $G(r)$ in (a) $Ca_3Ti_2O_7$, and (b) $Ca_{2.4}Sr_{0.6}Ti_2O_7$. Magnitude of the Ti-O dipoles approaches zero beyond T_d. (c) Schematic illustration of changes in dipolar correlations with increasing temperature (see text for description).

6(b) are that the local Ti-O dipoles drop to nearly zero for $T > T_d$, which explains the physical origin of the change in critical behavior at T_d. Below T_d, the local Ca/Sr-O and Ti-O dipoles are finite, and therefore correlations between these dipoles extend in three dimensions, although the correlation length decreases with increasing temperature. This gives rise to a scaling behavior for P, which is consistent with mean-field theory of phase transitions, that is, $\beta \sim 0.5$, for $T < T_d$. However, above T_d, the Ti-O dipole moments are vanishingly small. Therefore, above T_d, the dipolar correlations only extend along the Ca/Sr-O layers and interlayer dipolar correlations are significantly weaker—this gives rise to a scaling behavior, which is consistent with a 2D Ising universality class. The scenario is schematically illustrated in Fig. 6(c). This points to an important role for the B-O dipoles in cases where the B-site ion is ferroelectrically active, such as Ti in $(Ca, Sr)_3Ti_2O_7$. Although, the majority polarization component is from the A-O dipoles, the B-O dipoles play a critical role in interlayer dipolar coupling and hence enhanced total polarization at lower temperatures. Similarly, a large enhancement in polarization at lower temperatures was also reported for $Li_2SrNb_2O_7$, which contains ferroelectrically active Nb at the B site, although this point was not discussed in that article [18]. In contrast, for $A_3B_2O_7$ RP ferroelectrics with ferroelectrically inactive B-site ions such as Sn in $(Sr, Ca)_3Sn_2O_7$ [9] or Zr in $Sr_3Zr_2O_7$ [16], there is no transition point T_d for a sharp rise in polarization, and polarization increases monotonously below T_c.

III. CONCLUSION

In summary, from high-resolution neutron-scattering experiments, we clarified the evolution of the primary and secondary OPs for the paraelectric-ferroelectric phase transition in the HIFs $Ca_3Ti_2O_7$ and $Ca_{2.4}Sr_{0.6}Ti_2O_7$. The primary and the secondary order parameters are the octahedral tilt R and the polarization P, respectively. We observe that both R and P exhibit scaling behaviors, which are consistent with a 2D Ising universality class near T_c. However, we also identify

a second transition point $T_d < T_c$, below which P transforms from a 2D to a 3D universality class, which is driven by an increase in the Ti-O dipoles and therefore strengthening of the interlayer dipolar coupling. The current insights can enable rational design of site-specific chemistries in the RP phase and other layered perovskite HIFs for tuning of macroscopic polarization.

ACKNOWLEDGMENTS

The work described in this paper was partially supported by a grant from the Research Grants Council of the Hong Kong Special Administrative Region, China (Project No. eg CityU 11306720). J.K. and A.P. acknowledge support from the Research Talent Hub (RTH) program of the Innovation and technology Commission (ITC), Hong Kong. A portion of this research used resources at the Spallation Neutron Source, a DOE Office of Science User Facility operated by the Oak Ridge National Laboratory (Grant No. IPTS-27376 for POWGEN and NOMAD experiments). F.M. and M.R.V.J. thank the Danish Agency for Science, Technology, and Innovation for funding the instrument center DanScatt.

[1] M. E. Lines and A. M. Glass, *Principles and Applications of Ferroelectrics and Related Materials* (Oxford University Press, Oxford, UK, 1977).

[2] R. E. Cohen, Origin of ferroelectricity in perovskite oxides, Nature (London) **358**, 136 (1992).

[3] I. B. Bersuker, Jahn–Teller and pseudo-Jahn–Teller effects: From particular features to general tools in exploring molecular and solid state properties, Chem. Rev. **121**, 1463 (2021).

[4] J. F. Scott, Applications of modern ferroelectrics, Science **315**, 954 (2007).

[5] K. Uchino, *Ferroelectric Devices* (CRC Press, New York, 2019).

[6] N. A. Benedek and C. J. Fennie, Hybrid Improper Ferroelectricity: A Mechanism for Controllable Polarization-Magnetization Coupling, Phys. Rev. Lett. **106**, 107204 (2011).

[7] N. A. Benedek, J. M. Rondinelli, H. Djani, P. Ghosez, and P. Lightfoot,Understanding ferroelectricity in layered perovskites: New ideas and insights from theory and experiments, Dalton Trans. **44**, 10543 (2015).

[8] M. S. Senn, A. Bombardi, C. A. Murray, C. Vecchini, A. Scherillo, X. Luo, and S. W. Cheong, Negative Thermal Expansion in Hybrid Improper Ferroelectric Ruddlesden-Popper Perovskites by Symmetry Trapping, Phys. Rev. Lett. **114**, 035701 (2015).

[9] S. Yoshida, H. Akamatsu, R. Tsuji, O. Hernandez, H. Padmanabhan, A. S. Gupta, A. S. Gibbs, K. Mibu, S. Murai, J. M. Rondinelli, V. Gopalan, K. Tanaka, and K. Fujita, Hybrid improper ferroelectricity in $(Sr, Ca)_3Sn_2O_7$ and beyond: Universal relationship between ferroelectric transition temperature and tolerance factor in $n = 2$ Ruddlesden–Popper phases, J. Am. Chem. Soc. **140**, 15690 (2018).

[10] F. Pomiro, C. Ablitt, N. C. Bristowe, A. A. Mostofi, C. Won, S.-W. Cheong, and M. S. Senn, From first- to second-order phase transitions in hybrid improper ferroelectrics through entropy stabilization, Phys. Rev. B **102**, 014101 (2020).

[11] J. F. Scott, Fractal dimensions in switching kinetics of ferroelectrics, Ferroelectrics **349**, 157 (2007).

[12] W. Kleemann, J. Dec, and B. Westwanski, Susceptibility scaling behavior of quantum paraelectric $SrTiO_3$: Ca, Phys. Rev. B **58**, 8985 (1998).

[13] A. T. Mulder, N. A. Benedek, J. M. Rondinelli, and C. J. Fennie, Turning ABO_3 antiferroelectrics into ferroelectrics: Design rules for practical rotation-driven ferroelectricity in double perovskites and $A_3B_2O_7$ Ruddlesden-Popper compounds, Adv. Funct. Mater. **23**, 4810 (2013).

[14] G. J. Li, X. Q. Liu, J. J. Lu, H. Y. Zhu, and X. M. Chen, Crystal structural evolution and hybrid improper ferroelectricity in Ruddlesden-Popper $Ca_{3-x}Sr_xTi_2O_7$ ceramics, J. Appl. Phys. **123**, 014101 (2018).

[15] Y. S. Oh, X. Luo, F.-T. Huang, Y. Wang, and S.-W. Cheong, Experimental demonstration of hybrid improper ferroelectricity and the presence of abundant charged walls in $(Ca, Sr)_3Ti_2O_7$ crystals, Nat. Mater. **14**, 407 (2015).

[16] S. Yoshida, K. Fujita, H. Akamatsu, O. Hernandez, A. S. Gupta, F. G. Brown, H. Padmanabhan, A. S. Gibbs, T. Kuge, R. Tsuji, S. Murai, J. M. Rondinelli, V. Gopalan, and K. Tanaka, Ferroelectric $Sr_3Zr_2O_7$: Competition between hybrid improper ferroelectric and antiferroelectric mechanisms, Adv. Funct. Mater. **28**, 1801856 (2018).

[17] F.-T. Huang, B. Gao, J.-W. Kim, X. Luo, Y. Wang, M.-W. Chu, C.-K. Chang, H.-S. Sheu, and S.-W. Cheong, Topological defects at octahedral tilting plethora in bi-layered perovskites, npj Quantum Mater. **1**, 16017 (2016).

[18] R. Uppuluri, H. Akamatsu, A. S. Gupta, H. Wang, C. M. Brown, K. E. Agueda Lopez, N. Alem, V. Gopalan, and T. E. Mallouk, Competing polar and antipolar structures in the Ruddlesden–Popper layered perovskite $Li_2SrNb_2O_7$, Chem. Mater. **31**, 4418 (2019).

[19] M. Kratochvilova, F.-T. Huang, M.-T. Fernandez Diaz, M. Klicpera, S. J. Day, S. P. Thompson, Y.-S. Oh, B. Gao, S.-W. Cheong, and J.-G. Park, Mapping the structural transitions controlled by the trilinear coupling in $Ca_{3-x}Sr_xTi_2O_7$, J. Appl. Phys. **125**, 244102 (2019).

[20] X. Q. Liu, B. H. Chen, J. J. Lu, Z. Z. Hu, and X. M. Chen, Hybrid improper ferroelectricity in B-site substituted $Ca_3Ti_2O_7$: The role of tolerance factor, App. Phys. Lett. **113**, 242904 (2018).

[21] A. Huq, M. J. Kirkham, P. F. Peterson, J. P. Hodges, P. Whitfield, K. Page, T. Huegle, E. B. Iverson, A. Parizzi, and G. Q. Rennich, POWGEN: Rebuild of a third-generation powder diffractometer at the Spallation Neutron Source, J. Appl. Crystallogr. **52**, 1189 (2019).

[22] See Supplemental Material at http://link.aps.org/supplemental/10.1103/PhysRevB.107.224103 for detailed information about material preparation, measurement and fitting of neutron diffraction and total scattering patterns, crystallographic information, polarization calculation and SHG measurement.

[23] B. H. Toby and R. B. Von Dreele, GSAS-II: The genesis of a modern open-source all purpose crystallography software package, J. Appl. Crystallogr. **46**, 544 (2013).

[24] L. B. McCusker, R. B. Von Dreele, D. E. Cox, D. Louër, and P. Scardi, Rietveld refinement guidelines, J. Appl. Crystallogr. **32**, 36 (1999).

[25] R. Clarke and A. M. Glazer, The observation of critical behaviour in the thermal expansion of $PbZr_{0.9}Ti_{0.1}O_3$, J. Phys. C **7**, 2147 (1974).

[26] K. Deguchi and E. Nakamura, Breakdown of the Landau Theory in the Ferroelectric Phase Transition of Dicalcium Strontium Propionate, Phys. Rev. Lett. **37**, 1642 (1976).

[27] E. Almahmoud, I. Kornev, and L. Bellaiche, Critical Behavior in Ferroelectrics from First Principles, Phys. Rev. Lett. **102**, 105701 (2009).

[28] W. Kleemann, J. Dec, V. V. Shvartsman, Z. Kutnjak, and T. Braun, Two-Dimensional Ising Model Criticality in a Three-Dimensional Uniaxial Relaxor Ferroelectric with Frozen Polar Nanoregions, Phys. Rev. Lett. **97**, 065702 (2006).

[29] A. Glamazda, D. Wulferding, P. Lemmens, B. Gao, S.-W. Cheong, and K.-Y. Choi, Soft tilt and rotational modes in the hybrid improper ferroelectric $Ca_3Mn_2O_7$, Phys. Rev. B **97**, 094104 (2018).

[30] G. Jug, Critical behavior of disordered spin systems in two and three dimensions, Phys. Rev. B **27**, 609 (1983).

[31] J. M. Yeomans, *Statistical Mechanics of Phase Transitions* (Oxford University Press Inc., New York, 1992).

[32] T. Egami and S. J. L. Billinge, Underneath the Bragg peaks, *Structural Analysis of Complex Materials* (Elsevier, Oxford, 2003).

[33] J. Neuefeind, M. Feygenson, J. Carruth, R. Hoffmann, and K. K. Chipley, The nanoscale ordered materials diffractometer NOMAD at the spallation neutron source SNS, Nucl. Instrum. Methods. Phys. Res. Sect. B. **287**, 68 (2012).

[34] C. L. Farrow, P. Juhas, J. W. Liu, D. Bryndin, E. S. Bozin, J. Bloch, T. Proffen, and S. J. L. Billinge, PDFfit2 and PDFgui: Computer programs for studying nanostructure in crystals, J. Phys.: Condens. Matter **19**, 335219 (2007).

[35] J. Kong, L. Li, J. Liu, F. P. Marlton, M. R. V. Jorgensen, and A. Pramanick, A local atomic mechanism for monoclinic-tetragonal phase boundary creation in Li-doped $Na_{0.5}K_{0.5}NbO_3$ ferroelectric solid solution, Inorg. Chem. **61**, 4335 (2022).